The Astrophysical Journal, 980:46 (12pp), 2025 February 10 https://doi.org/10.3847/1538-4357/ad9de5

A Search for Radio Millisecond Pulsar Companions around Extremely Low-mass White Dwarfs with Ellipsoidal Variability

W. J. Huang[1], Pak-Hin Thomas Tam[1], L. L. Ren[2], and J. M. Lin[1]

[1] School of Physics and Astronomy, Sun Yat-sen University, Zhuhai 519082, People's Republic of China; tanbxuan@mail.sysu.edu.cn

[2] School of Electrical and Electronic Engineering, Anhui Science and Technology University, Bengbu, Anhui 233030, People's Republic of China

Received 2024 May 30; revised 2024 December 7; accepted 2024 December 10; published 2025 February 3

Abstract

Extremely low-mass (ELM) white dwarfs (WDs) are helium-core WDs with masses less than 0.3 $M_\odot$. Short-period ELM WD binaries that exhibit ellipsoidal variations may harbor heavier companions, either massive WDs or millisecond pulsars (MSPs). In this study, we selected ~12,000 ELM WDs or their candidates, and searched for ellipsoidal-like lightcurves with orbital periods shorter than 1 day, by using the public data from Zwicky Transient Facility. Finally, 23 such systems were found, with 17 being newly discovered. We selected nine high-priority targets likely to evolve from the Roche lobe overflow channel and estimated their companion masses from the extracted ellipsoidal variation amplitude. Among them, four targets have companion masses exceeding 1 $M_\odot$. We performed a search for radio pulsations from six of these targets by using Five-hundred-meter Aperture Spherical radio Telescope. However, no convincing radio pulse signals were found, resulting in upper limits for the radio flux at around 8 μJy. Given the nondetection of radio pulsations from a total of 11 similar systems, the fraction of ellipsoidal ELM WDs around MSPs is estimated to be below $15^{+6}_{-3}\%$. We anticipate that multiwavelength studies of more ellipsoidal-like ELM WDs will further constrain the fraction.

Unified Astronomy Thesaurus concepts: White dwarf stars (1799); Millisecond pulsars (1062); Ellipsoidal variable stars (455); Close binary stars (254)

1. Introduction

Extremely low-mass (ELM) white dwarfs (WDs) are commonly considered as helium-core WDs with masses less than ~0.3 $M_\odot$. Generally, these systems can exclusively originate within close binaries since the age of the Universe has not allowed isolated stars to form ELM WDs. The surface hydrogen envelope of the ELM WD's progenitor is stripped away by the companion star, through a stable Roche lobe overflow (RLO) or common envelope (CE) ejection channel (M. Sun & P. Arras 2018; Z. Li et al. 2019), preventing the conditions necessary for a helium flash and leading to the formation of a low-mass helium-core WD.

Most ELM WDs have been discovered in the ELM Survey, which carried out follow-up spectroscopic measurements for ELM WD targets based on photometric selections (e.g., W. R. Brown et al. 2010; W. R. Brown et al. 2016, 2020, 2022). Currently, the ELM Survey has identified about 150 low-mass WD binaries covering the Southern and Northern Hemispheres and has found over a dozen ultracompact WD binaries ($P_{\rm orb} \leqslant 1$ hr), which are potential multimessenger sources that emit gravitational waves at millihertz frequencies (A. Kosakowski et al. 2023a). These are also leading targets detectable by space-based gravitational wave observatories such as LISA (T. Kupfer et al. 2018) and TianQin (S.-J. Huang et al. 2020). Additionally, some studies are dedicated to searching for the more bloated pre-ELM WDs that have not yet begun their cooling track evolution (K. El-Badry et al. 2021; H. Yuan et al. 2023).

Almost all known ELM WDs are binary systems, and their companions typically encompass millisecond pulsars (MSPs; A. G. Istrate et al. 2014a), type A or F dwarfs (EL CVn-type binaries; P. F. L. Maxted et al. 2014), and in most instances, WDs (W. R. Brown et al. 2020). Generally, MSPs are recycled pulsars that accrete mass and transfer angular momentum from their companions during the phase of being low-mass X-ray binaries, while most donors eventually become low-mass He-core WDs (T. M. Tauris & G. J. Savonije 1999; M. H. van Kerkwijk et al. 2005). At present, the ATNF pulsar catalog contains over 600 MSPs (spin period $P_{\rm spin} < 30$ ms), of which approximately 200 are in binary systems with WDs (R. N. Manchester et al. 2005). By combining the mass function obtained from the MSP spin Doppler effect, it is estimated that the number of MSP/ELM WD systems is roughly 140, assuming a neutron star (NS) mass of 1.35 $M_\odot$ and an orbital inclination of 60°. These systems almost all have circular orbits, with orbital periods ranging from 0.05 to 669 days. It is important to emphasize that the recycled MSP orbiting the WD may be more massive (M. Linares 2020), which would result in a greater estimated mass for the companion star.

In fact, on the one hand, the masses of both components in some rare MSP binaries can be accurately estimated through radio timing measurements involving Shapiro delay (e.g., P. B. Demorest et al. 2010) and periastron precession (e.g., P. C. C. Freire et al. 2008). On the other hand, if the WD around MSPs is accessible for detailed spectroscopic measurements, its mass can be derived by comparing the atmospheric parameters with the mass–radius relations of low-mass WDs. The pulsar's mass can then be determined by jointly analyzing the WD's radial velocity variations and the pulsar timing results (M. H. van Kerkwijk et al. 2005).

However, the majority of WDs around MSPs are too faint for optical observations (M. H. van Kerkwijk et al. 2005;

M. A. Agüeros et al. 2009; J. Antoniadis 2021). So far, only about a handful of MSP/ELM WD systems have been confirmed through either radio timing analysis or optical identification, such as MSP J0218+4232 (C. G. Bassa et al. 2003), J0348+0432 (J. Antoniadis et al. 2013), J0437-4715 (J. P. W. Verbiest et al. 2008; M. Durant et al. 2012), J0614-3329 (C. G. Bassa et al. 2016), J0751+1807 (G. Desvignes et al. 2016), J1012+5307 (M. H. van Kerkwijk et al. 1996), J1713+0747 (E. M. Splaver et al. 2005), J1738+0333 (J. Antoniadis et al. 2012), J1857+0943 (M. H. van Kerkwijk et al. 2000; Z. Arzoumanian et al. 2018), J1909-3744 (B. A. Jacoby et al. 2005), and J1911-5958A (C. G. Bassa et al. 2006). Specifically, the first ELM WD was identified spectroscopically as the companion to the PSR J1012+5307 (M. H. van Kerkwijk et al. 1996; D. Mata Sánchez et al. 2020; N. Wei et al. 2024). PSR J1738+0333 was the first MSP discovered alongside a pulsating ELM WD companion, exhibiting multimode pulsation periods ranging from 1790 s to 9860 s (M. Kilic et al. 2015; M. Kilic et al. 2018). In addition, since approximately 35% of MSPs are located in globular clusters, high-resolution optical telescopes are also highly effective for identifying MSP/ELM WD systems, which can provide valuable insights into the dynamical evolution of MSP binaries (e.g., M. Cadelano et al. 2015, 2019).

Enlarging the population of compact MSP/ELM WD systems is important to investigate the recycling scenario of MSPs as well as stellar binary evolution (e.g., A. G. Istrate et al. 2014a, 2014b, 2016). Particularly, once the ELM WD companions to MSPs are bright enough, their optically dependent photometric and spectroscopic measurements (such as atmospheric parameters, radial velocity variations, parallax, and cooling age) can indirectly improve or constrain estimates for some fundamental parameters of MSPs, including mass, distance, age, and more (e.g., M. H. van Kerkwijk et al. 2005; J. Antoniadis et al. 2013). Many studies (J. van Leeuwen et al. 2007; M. A. Agüeros et al. 2009; W. R. Brown et al. 2020; T. M. Athanasiadis et al. 2021) have tried to search for radio MSPs around the position of low-mass WDs with high mass functions. However, no pulsar signals were detected and the fraction of low-mass WDs orbited by NSs was estimated to be below 10% (T. M. Athanasiadis et al. 2021).

ELM WDs exhibit larger sizes and higher brightness compared to other WDs, due to the inverse correlation between mass and radius (K. Wang et al. 2022). They are more prone to being tidally distorted by their heavier companions (typically MSPs or CO-core WDs) in close binary systems. This distortion often leads to observable ellipsoidal variability since their projected sizes change as they orbit (e.g., J. J. Hermes et al. 2014; K. I. I. Koljonen & M. Linares 2023). Because the amplitude of ellipsoidal variation is roughly proportional to $(M_2/M_1)(R_1/a)^3$, where M_1 and M_2 are the masses of the optical primary (ELM WD) and the unseen secondary respectively, a denotes the orbital semimajor axis and R_1 is the primary's radius (J. J. Hermes et al. 2014), MSP/ELM WD binaries seem to be more likely to exhibit ellipsoidal variability compared to double WDs in similar orbits. Therefore, searching for tidally distorted ELM WDs can provide one of the clues for finding potential MSPs. Meanwhile, modeling the ellipsoidal variability of ELM WDs can also constrain the system's inclination and companion mass (J. J. Hermes et al. 2014; K. J. Bell et al. 2018).

In this work, we aim to identify ellipsoidal-like lightcurves of ELM WDs with orbital periods shorter than 1 day, and further analyze whether these systems harbor MSPs through targeted radio observations. The structure of the paper is outlined as follows: In Section 2, we introduce the selection of ELM WD samples. In Section 3, we describe the identification of ellipsoidal lightcurves. The results will be presented in Section 4. In Section 5, we discuss the fraction of ellipsoidal ELM WDs containing MSPs, and Section 6 presents the final conclusion.

2. Sample Selection

The ongoing Gaia astrometric survey now presents extraordinary opportunities for discovering more faint ELM WDs. Here, we adopt three representative catalogs obtained from previous publications based on the analysis of Gaia DR2 and EDR3 data, as our ELM WD samples or candidates for further study:

1. Over the course of more than 10 yr, the ELM Survey has conducted spectroscopic measurements, obtaining a large data set of known low-mass WDs as well as their orbital and stellar atmospheric parameters. We select 119[3] ELM WDs (hereafter referred to as sample S1) with a mass cutoff of 0.3 $M_\odot$ from the ELM Survey (W. R. Brown et al. 2020, 2022).
2. By applying a series of color cuts in the Hertzsprung–Russell diagram while considering the distribution of known ELM WDs and evolutionary model, I. Pelisoli & J. Vos (2019) identified a sample of 5762 ELM WD candidates[4] (hereafter referred to as sample S2) selected from Gaia DR2.
3. N. P. Gentile Fusillo et al. (2021) provided a comprehensive catalog including 1,280,266 WD candidates[5] from Gaia EDR3 by using some selection criteria. They also estimated the probability of being a WD ($P_{\rm WD}$) for them and derived various stellar parameters, such as effective temperature, surface gravity, and mass. To select the high-confidence ELM WDs, we establish the following criteria: (i) all three types of masses ($\texttt{mass}_{\rm H}$, $\texttt{mass}_{\rm He}$, $\texttt{mass}_{\rm mixed}$) derived from different atmospheric models (pure-H models, pure-He and mixed models) are below 0.3 $M_\odot$, and (ii) the probability $P_{\rm WD}$ is larger than 0.75. This selection process yields 6823 ELM WD candidates (hereafter referred to as sample S3). It's worth noting that mass values less than 0.2 $M_\odot$ may not be accurate because those parameters are inferred from an invalid range of mass–radius relations (N. P. Gentile Fusillo et al. 2021).

After removing overlapping sources from the three samples, we finally obtained a sample comprising ∼12,000 ELM WDs or their candidates.

3. Lightcurve Selection

3.1. Periodic Signal Search

The Zwicky Transient Facility (ZTF; E. C. Bellm et al. 2019; M. J. Graham et al. 2019; F. J. Masci et al. 2019) is a time-

---

[3] The original sample of low-mass WDs is sourced from Table 2 in W. R. Brown et al. (2020) and Table 1 in W. R. Brown et al. (2022). The number of ELM WDs selected below 0.3 $M_\odot$ in these two tables is 105 and 14, respectively. The complete Table 2 in W. R. Brown et al. (2020) can be found at https://cdsarc.cds.unistra.fr/viz-bin/cat/J/ApJ/889/49.

[4] https://cdsarc.cds.unistra.fr/viz-bin/cat/J/MNRAS/488/2892#/browse

[5] https://warwick.ac.uk/fac/sci/physics/research/astro/research/catalogs/

domain astronomical survey covering the sky north of −28° decl. The employed Palomar 48-inch Schmidt telescope (FoV $\sim 47\ \mathrm{deg}^2$) scans the entire northern sky every two nights in multiband filters (g, r, i) with a limiting magnitude of detection down to ∼21. At present, ZTF has been widely applied in the search for periodic lightcurves of WDs (e.g., K. El-Badry et al. 2021; P. M. Keller et al. 2021; L. Ren et al. 2023).

We query lightcurve data from ZTF DR15 for each coordinate within 1″. Because ZTF-i data are recorded less frequently, we exclusively analyze sources that have both ZTF-g and ZTF-r data. As a result, nearly 7000 targets are available for further analyze. The period search range spans from 5 minutes to 1 day, within which there is a higher likelihood of discovering ellipsoidal variations. We employ the Lomb–Scargle (LS) algorithm from `Astropy`[6] to search for sinusoidal-like ellipsoidal lightcurves. If the ZTF-g and ZTF-r data display similar maximum LS power in their power spectra, indicating the same most prominent period ("LS period" thereafter), these sources will be deemed to have reliable periodic signals.

3.2. Lightcurve Identification

During the search process, we encountered many lightcurves with diverse characteristics, and the six primary types are presented in Figure 1. They are reflection binaries, ellipsoidal binaries (hereafter ELL-type binaries), and eclipsing binaries, including four subclasses: HW Vir-type binaries, eclipsing WD +MS systems, EA-type binaries, and EB-type binaries. Eclipsing binary systems commonly exhibit extremely sharp dips in the lightcurves, and their shapes depend on the sizes and separation of two stars, their temperatures, the inclination of the orbital plane and other factors. Their orbital periods are typically one or two times the LS period. See K. El-Badry et al. (2021) and L. Ren et al. (2023) for more details about these eclipsing systems. In addition, it is unlikely for eclipsing binaries to harbor an NS.

The non-eclipsing reflection binary generally consists of an M dwarf and a hot WD (K. El-Badry et al. 2021). The M dwarf heated on one side displays a quasi-sinusoidal modulation in its reflected light. Meanwhile, their variability amplitudes in the g band are notably lower compared to those in the r band due to a substantial portion of the optical light being contributed by the hot WD. Their orbital periods are directly determined by the LS period.

K. El-Badry et al. (2021) suggest the ellipsoidal lightcurves should exhibit double-peak features as well as unequal brightness minima caused by gravity darkening. However, the gravity-darkening effect may not be readily apparent, or can be counteracted by other factors, such as heating from their companions. Similar examples can be seen in other ellipsoidal-like variables (J. J. Hermes et al. 2014; K. I. I. Koljonen & M. Linares 2023; A. Kosakowski et al. 2023a), or J0745+1949 shown in Figure 2. We are not solely aiming to search for pure ellipsoidal variables in order to preserve a greater number of potential samples. Thus, alternating brightness minima is excluded in the selection criteria of this work. Of course, this may also involve some interference sources, such as single-mode pulsators and rotators whose lightcurves are similar to ellipsoidal variables with equal minima.

On the other hand, the highest peak in the LS power spectrum often identifies half the orbital period of the ELL-type lightcurve, while the power corresponding to the true period is mostly not prominent unless asymmetric double peaks in the lightcurve caused by Doppler beaming effect is present (e.g., J. J. Hermes et al. 2014; W. R. Brown et al. 2022). Based on this phenomenon, we directly fold the time series at twice the LS period to reconstruct their double-peak structures in the lightcurves.

Due to the absence of alternating minima in the lightcurve and the lack of a distinct peak corresponding to the orbital period in the LS power spectrum, we mainly distinguish between reflection systems and ellipsoidal variables based on the difference in the amplitude variation of their g-band and r-band lightcurves, since the latter have similar variability amplitudes in both bands. Thus, we proceed as follows.

First, phase-folded lightcurves of double bands are binned into 100 orbital phase points. We assume the epoch ($T_{0,\mathrm{sup\_conj}}$) of the minimum g-band flux as the common zero phase point, corresponding to the superior conjunction of the ELM WD. Specifically, for double-peaked lightcurves with different peak heights, possibly due to the Doppler beaming effect, we designate the highest peak as phase 0.25. We then employ a nonlinear least-squares fit that includes an offset and the amplitude of the ellipsoidal variations ($\cos 2\phi$), Doppler beaming ($\sin \phi$), reflection ($\cos \phi$), the first harmonic of the orbital period ($\sin 2\phi$) (J. J. Hermes et al. 2014). Next, we calculate the difference in peak-to-peak amplitudes of double-band lightcurves. Here, we define the peak-to-peak amplitude as the difference between the maximum and minimum value of the fitted curve obtained from the five-parameter model. When the difference in peak-to-peak amplitudes of two bands is comparable to the average error of lightcurve data, we consider it to be an ellipsoidal-like variable rather than a reflection system.

Finally, we obtained 23 ELM WDs or candidates exhibiting ellipsoidal variability (see Figure 2), with seven sources from sample S1, 17 sources from sample S2, and three sources from sample S3. Additionally, 17 sources of them are newly discovered to exhibit ellipsoidal variability. Their main parameters are listed in Table 1.

4. Results

4.1. Distribution in the Color–Magnitude Diagram

Figure 3 depicts the distribution of 23 ELM WDs or their candidates in a Gaia color–magnitude diagram (CMD). They all fall between the main sequence stars and WDs, within the region recommended by J. Antoniadis (2021) for locating low-mass WDs companions to MSPs. For comparison, the search region of the ELM survey (A. Kosakowski et al. 2023a) and the region suggested by I. Pelisoli & J. Vos (2019) for finding ELM WDs are also plotted on the CMD. The former represents the distribution of most known ELM WDs to date, while the irregular region of the latter can effectively distinguish ELM WD candidates from the surrounding higher mass WDs, hot subdwarfs, and scattered main sequence stars. The majority of our sources also fall within these regions.

4.2. High-priority ELM WD Candidates

The effective temperature and surface gravity of the sample listed in Table 1 span a wide range, with some candidates likely

---

[6] https://docs.astropy.org/en/stable/timeseries/lombscargle.html

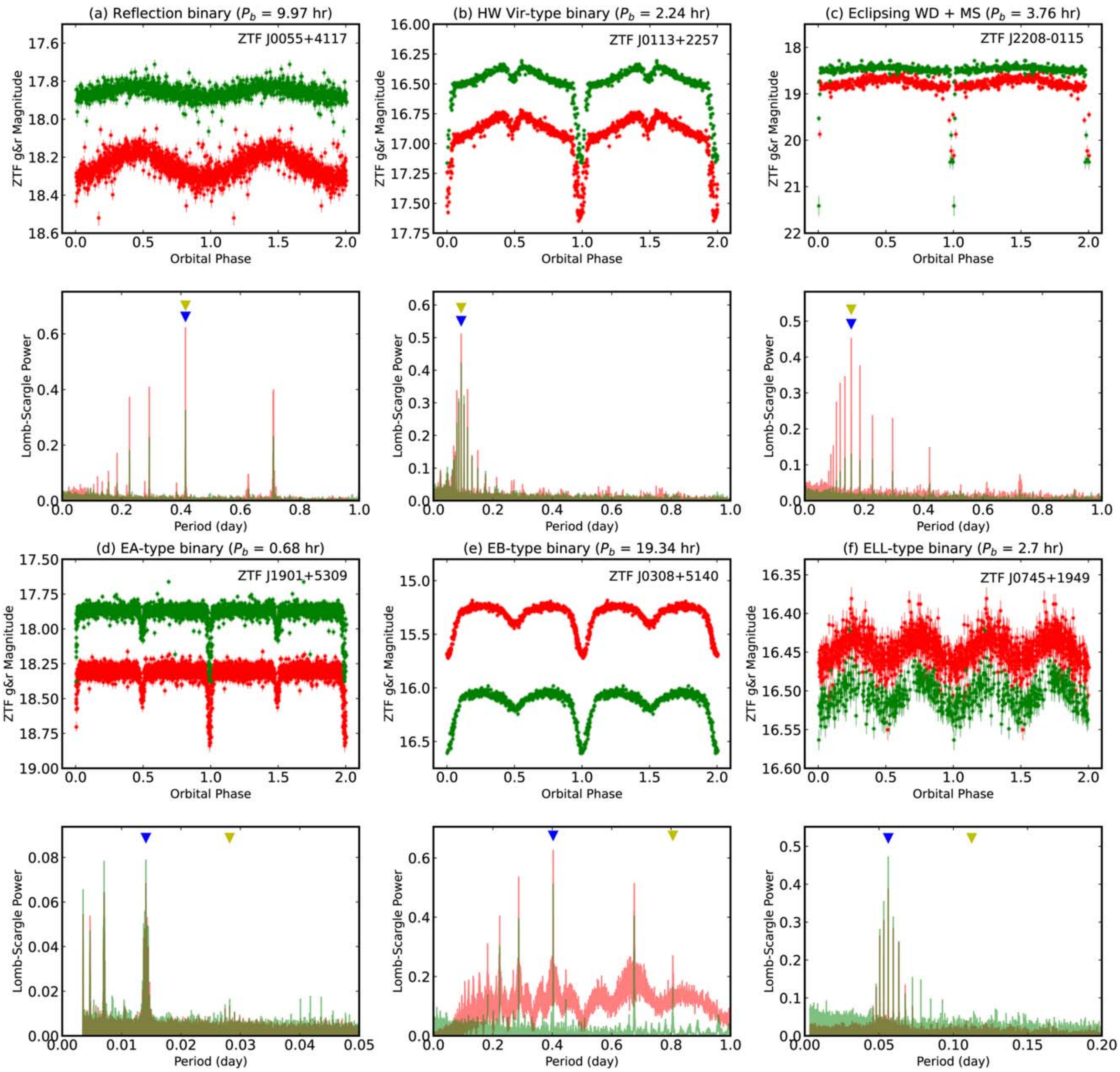

Figure 1. Six primary types of lightcurves ((a)–(f)) found in our ELM WD samples. ZTF-g and ZTF-r data are represented in green and red, respectively. The panel below each type of lightcurve presents the LS power spectra obtained from ZTF-g and ZTF-r data. The blue inverted triangle marks the LS period with the maximum power, while the yellow inverted triangle marks the period at which the lightcurve is actually folded.

belonging to sdA stars ($\log g_1 \sim 6$ and $T_{\rm eff} < 9000$ K) (W. R. Brown et al. 2017) or sdB stars ($25{,}000\,{\rm K} < T_{\rm eff} < 40{,}000$ K and $5 < \log g_1 < 6$) (U. Heber 2009). W. R. Brown et al. (2020) employed a relatively narrow selection criterion with $8800\,{\rm K} \lesssim T_{\rm eff} \lesssim 22{,}000$ K and $5.5 \lesssim \log g_1 \lesssim 7.1$ to identify clean samples of ELM WDs. However, under this criterion, only three sources in our sample meet the requirements. To increase the number of ELM WD candidates for further analysis, we select objects with well-measured atmospheric parameters, whose effective temperatures and surface gravities fall within the broader ranges of $8000\,{\rm K} \lesssim T_{\rm eff} \lesssim 22{,}000$ K and $5 \lesssim \log g_1 \lesssim 7$, as recommended by W. R. Brown et al. (2016) for the empirical range of ELM WDs. The total of nine selected targets is listed in Table 2.

We then carefully compared their spectrophotometric parallaxes, inferred from the evolutionary tracks of ELM WDs, with the Gaia parallaxes. If the difference between the two does not exceed a factor of 3, the object can be considered a high-priority ELM WD candidate (W. R. Brown et al. 2020; K. Wang et al. 2022). The comparison results are shown in Figure 4. As seen, except for J0745+1949, all other sources fall between the 1:3 ratio line and the 3:1 ratio line, and can be considered good candidates.

The two cooler (<9000 K) ELM WDs, J1048-0000 and J1401-0817, fall below the 1:1 ratio line and exhibit relatively large deviations, somewhat similar to sdA-type stars. This can be interpreted as either the inflation of the radii or systematic errors in surface gravity (W. R. Brown et al. 2017, 2020). K. El-Badry et al. (2021) argued that the $\log g_1$ for J1401-0817 should be 4.93 ± 0.1, rather than the overestimated reported value (∼5.731), in order to account for the observed significant amplitude of ellipsoidal variability. The situation for J1048-0000 is likely similar. If their actual $\log g_1$ values are indeed

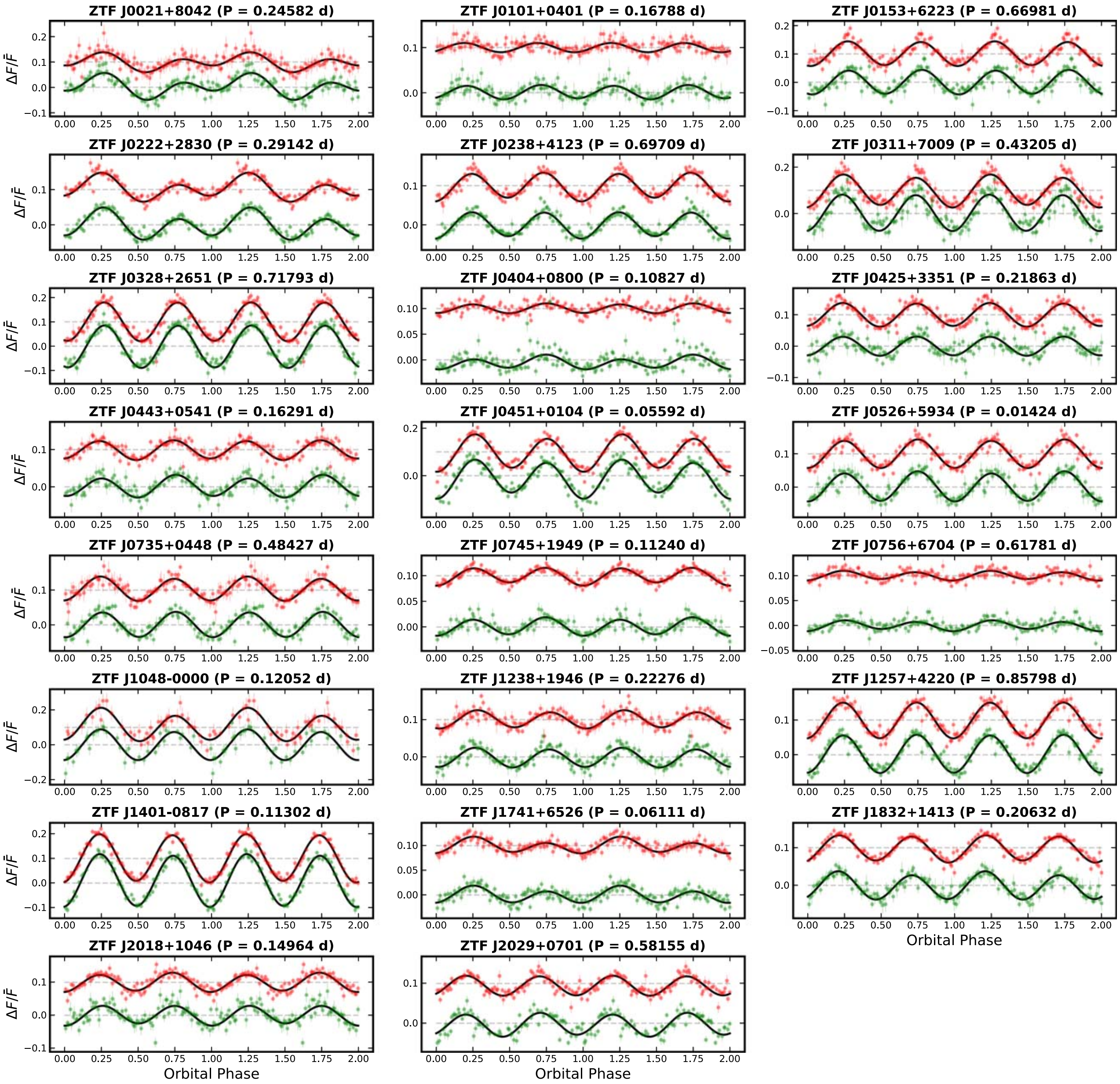
ZTF J0021+8042 (P = 0.24582 d)
ZTF J0101+0401 (P = 0.16788 d)
ZTF J0153+6223 (P = 0.66981 d)
ZTF J0222+2830 (P = 0.29142 d)
ZTF J0238+4123 (P = 0.69709 d)
ZTF J0311+7009 (P = 0.43205 d)
ZTF J0328+2651 (P = 0.71793 d)
ZTF J0404+0800 (P = 0.10827 d)
ZTF J0425+3351 (P = 0.21863 d)
ZTF J0443+0541 (P = 0.16291 d)
ZTF J0451+0104 (P = 0.05592 d)
ZTF J0526+5934 (P = 0.01424 d)
ZTF J0735+0448 (P = 0.48427 d)
ZTF J0745+1949 (P = 0.11240 d)
ZTF J0756+6704 (P = 0.61781 d)
ZTF J1048-0000 (P = 0.12052 d)
ZTF J1238+1946 (P = 0.22276 d)
ZTF J1257+4220 (P = 0.85798 d)
ZTF J1401-0817 (P = 0.11302 d)
ZTF J1741+6526 (P = 0.06111 d)
ZTF J1832+1413 (P = 0.20632 d)
ZTF J2018+1046 (P = 0.14964 d)
ZTF J2029+0701 (P = 0.58155 d)

Figure 2. Phase-folded, binned lightcurves in the ZTF-*g* band (green) and ZTF-*r* band (red) for 23 ellipsoidal-like variables identified in this work. The *r*-band lightcurves are vertically shifted upward by 0.1 for clarity. The black solid lines denote the best-fit curves obtained from the five-parameter model.

smaller than the reported ones, their larger radii would bring the spectrophotometric parallax estimates closer to the Gaia parallaxes. The estimated parallax of J0745+1949 shows the largest deviation from the Gaia parallax, suggesting that its mass or radius, as derived from the ELM WD evolutionary model, may be incorrect. In fact, J0745+1949 exhibits abundant metal lines, indicating that it may have recently experienced a CNO flash and might not yet be on the final cooling track (A. Gianninas et al. 2014; J. J. Hermes et al. 2014). This characteristic is somewhat similar to that of the companion of PSR J1816+4510, which is believed to be a low-mass proto-WD (D. L. Kaplan et al. 2012; D. L. Kaplan et al. 2013; A. G. Istrate et al. 2014b). Therefore, we retain J0745+1949 as a "high-priority" candidate for investigating the potential presence of a pulsar through studies at other wavelengths. Notably, J0756+6704 is a pre-ELM WD exhibiting *p*-mode pulsations with periods of 521 s and 587 s (A. Gianninas et al. 2016). Its T_{eff} and $\log g_1$ differ from those derived by W. R. Brown et al. (2020), whose estimated parallax (∼1.443) shows a notable deviation from the Gaia parallax.

We also investigate the possible counterparts of other non-high-priority sources listed in Table 1, although most still require detailed spectroscopic measurements for further confirmation of their nature. J0153+6223, J0222+2830, J0425+3351, and J0735+0448are high-probability ($P_{\mathrm{WD}} > 0.75$) low-mass WD candidates in the WD catalog of N. P. Gentile Fusillo et al. (2021). It is worth noting that the T_{eff} and $\log g_1$ of J0222+2830 also meet the criteria for an ELM WD, and its spectrophotometric parallax is approximately 4.652 ± 0.577, as estimated using the given atmospheric parameters and the method described by K. Wang et al. (2022). This value is very close to the Gaia parallax (∼4.386). By checking the Gaia DR3 source ID in SIMBAD,[7] it may also correspond to KUV 02196+2816, which is considered to be a double-degenerate WD

---

[7] https://simbad.u-strasbg.fr/simbad/

Table 1

Astrometric and Atmospheric Parameters of 23 ELL-type Targets

Name	R.A. (hh:mm:ss.ss)	Decl. (dd:mm:ss.s)	bp − rp (mag)	G (mag)	Parallax (mas)	Period (d)	$T_{\rm eff}$ (K)	log g_1 (cm s^{-2})	M_1 ($M_\odot$)	References	Sample
ZTF J0021+8042*	00:21:13.50	+80:42:35.3	−0.376	17.974	1.168 ± 0.097	0.24582	…	…	…	…	S2
ZTF J0101+0401*	01:01:28.69	+04:01:59.0	0.156	17.293	0.796 ± 0.098	0.16788	9284^{+120}_{-120}	$5.229^{+0.089}_{-0.089}$	0.188 ± 0.013	(1)	S1, S2
ZTF J0153+6223*	01:53:06.26	+62:23:19.2	0.009	17.997	2.332 ± 0.100	0.66981	$23, 343^{+1835}_{-1835}$	$7.265^{+0.142}_{-0.142}$	0.387 ± 0.039	(2)	S2
ZTF J0222+2830*	02:22:28.37	+28:30:7.6	0.069	17.056	4.386 ± 0.114	0.29142	$10, 485^{+290}_{-290}$	$6.785^{+0.087}_{-0.087}$	0.211 ± 0.019	(2)	S3
ZTF J0238+4123*	02:38:24.05	+41:23:20.4	−0.460	17.329	1.008 ± 0.101	0.69709	$80, 210^{+12440}_{-12440}$	$6.246^{+0.333}_{-0.333}$	…	(3)	S2
ZTF J0311+7009*	03:11:10.40	+70:09:41.9	0.013	18.311	1.557 ± 0.144	0.43205	…	…	…	…	S2
ZTF J0328+2651*	03:28:03.02	+26:51:51.6	−0.229	18.179	1.524 ± 0.186	0.71793	9077^{+311}_{-45}	$4.620^{+0.007}_{-0.005}$	0.169 ± 0.003†	(4)	S2
ZTF J0404+0800*	04:04:18.39	+08:00:02.9	0.348	15.945	1.742 ± 0.044	0.10827	$10, 860^{+120}_{-120}$	$4.985^{+0.121}_{-0.121}$	0.172 ± 0.014	(3)	S2
ZTF J0425+3351*	04:25:11.52	+33:51:29.6	0.081	18.310	2.683 ± 0.188	0.21863	$19, 653^{+3265}_{-3265}$	$7.384^{+0.267}_{-0.267}$	0.394 ± 0.076	(2)	S2
ZTF J0443+0541*	04:43:02.66	+05:41:17.0	0.297	17.289	0.760 ± 0.085	0.16291	9390^{+140}_{-140}	$4.998^{+0.097}_{-0.097}$	0.159 ± 0.013	(3)	S2
ZTF J0451+0104	04:51:16.84	+01:04:26.2	0.516	15.344	3.406 ± 0.033	0.05592	…	…	…	…	S2
ZTF J0526+5934	05:26:10.42	+59:34:45.3	0.186	17.563	1.183 ± 0.091	0.01424	$27, 300^{+260}_{-260}$	$6.37^{+0.03}_{-0.03}$	0.380 ± 0.067	(5)	S2
ZTF J0735+0448*	07:35:29.47	+04:48:48.8	−0.328	17.570	1.055 ± 0.103	0.48427	$25, 555^{+3078}_{-3078}$	$6.475^{+0.242}_{-0.242}$	0.227 ± 0.028	(2)	S2, S3
ZTF J0745+1949	07:45:11.56	+19:49:26.6	0.384	16.406	1.088 ± 0.059	0.11240	8313^{+100}_{-100}	$6.151^{+0.074}_{-0.074}$	0.160 ± 0.010	(6)	S1, S2
ZTF J0756+6704*	07:56:10.73	+67:04:24.4	0.035	16.410	0.484 ± 0.046	0.61781	$11,640^{+250}_{-250}$	$4.90^{+0.14}_{-0.14}$	0.181 ± 0.011	(7)	S1
ZTF J1048-0000*	10:48:26.86	−00:00:56.8	0.325	18.247	0.641 ± 0.195	0.12052	8484^{+90}_{-90}	$5.831^{+0.051}_{-0.051}$	0.169 ± 0.016	(6)	S1
ZTF J1238+1946*	12:38:00.08	+19:46:31.1	−0.144	17.487	0.452 ± 0.099	0.22276	$14, 950^{+420}_{-420}$	$4.890^{+0.050}_{-0.050}$	0.197 ± 0.012	(6)	S1, S2
ZTF J1257+4220	12:57:23.99	+42:20:53.5	−0.401	17.442	1.154 ± 0.109	0.85798	$43, 974^{+347}_{-347}$	$7.612^{+0.037}_{-0.037}$	0.524 ± 0.003	(8)	S3
ZTF J1401-0817	14:01:18.80	−08:17:23.5	0.243	16.663	0.823 ± 0.079	0.11302	8813^{+90}_{-90}	$5.731^{+0.048}_{-0.048}$	0.216 ± 0.042	(6)	S1
ZTF J1741+6526	17:41:40.49	+65:26:38.6	0.145	18.456	0.867 ± 0.143	0.06111	$10, 540^{+170}_{-170}$	$6.000^{+0.060}_{-0.060}$	0.170 ± 0.010	(6)	S1
ZTF J1832+1413*	18:32:45.51	+14:13:11.3	0.589	17.454	0.665 ± 0.092	0.20632	6862^{+49}_{-17}	$4.473^{+0.010}_{-0.010}$	…	(4)	S2
ZTF J2018+1046*	20:18:9.99	+10:46:47.1	0.459	17.436	0.829 ± 0.089	0.14964	8216^{+115}_{-154}	$4.427^{+0.042}_{-0.075}$	0.167 ± 0.005†	(4)	S2
ZTF J2029+0701*	20:29:32.52	+07:01:7.7	−0.411	16.624	1.915 ± 0.068	0.58155	$63, 102^{+16916}_{-16916}$	$7.437^{+0.172}_{-0.172}$	0.519 ± 0.047	(2)	S2

Note. The source name with "*" indicates it is a newly discovered ellipsoidal-like variable in this paper. The values of coordinates (R.A.,decl.), BP − RP color (bp − rp), G-band mean magnitude (G) and parallax are provided from Gaia DR3. The orbital periods are obtained from the ZTF lightcurves. The effective temperature ($T_{\rm eff}$), surface gravity (log g_1), and WD mass (M_1) are directly collected from existing publications or Gaia DR3, shown in the References column. An exception is that the masses of two WDs, marked with "†," are derived from L. G. Althaus et al. (2013), through bilinear interpolation of the $T_{\rm eff}$ and log g_1 given by Gaia DR3, which may not be entirely accurate. The column Sample indicates the sample from which each source originates.**References.** (1) W. R. Brown et al. (2022) (2) N. P. Gentile Fusillo et al. (2021) (3) K. Wang et al. (2022) (4) Gaia DR3 (5) A. Kosakowski et al. (2023a) (6) W. R. Brown et al. (2020) (7) A. Gianninas et al. (2015) (8) S. O. Kepler et al. (2019).

system containing a DA star and a DB star (M. M. Limoges et al. 2009).

J2029+0701 is also a high-probability WD, although its high temperature (~63,000 K) and ~0.5 $M_\odot$ mass seem to correspond to a canonical sdB-type star. N. P. Gentile Fusillo et al. (2021) pointed out that parameters above 40,000 K are unreliable and require further spectroscopic observations for confirmation. J1257+4220 was classified as a hot DA-type WD with UHE lines, and it is possibly a binary system (S. O. Kepler et al. 2019; N. Reindl et al. 2021). J0238+4123 has the highest effective temperature (~80,000 K), making it seem to be a hot sdB-type star. The photometric variability of J0451+0104 and J0526+5934 was first discovered by L. Ren et al. (2023), and they are potential gravitational wave candidates with orbital periods under 100 minutes. In particular, J0526+5934, with an orbital period of only 40 minutes, is identified as a low-mass WD or post-core-burning hot subdwarf, accompanied by a massive CO-core WD (A. Kosakowski et al. 2023b; A. Rebassa-Mansergas et al. 2024). The remaining five either have missing atmospheric parameters or parameters provided only by Gaia DR3, necessitating further spectroscopic measurements and studies for identification.

4.3. Mass–Period Distribution

ELM WDs may form through either the CE channel or the RLO channel, as suggested by binary evolution theory. However, it is improbable that ELM WDs with MSPs are formed via the CE channel, as NSs are unable to accrete sufficient material to become MSPs (Z. Li et al. 2019). The mass–period diagram provides a clear reflection of the formation channel of ELM WDs.

Figure 5 illustrates the distribution of nine high-priority ELL-type ELM WDs on the mass–period diagram, shown by the open red square. Some confirmed ELM WDs orbiting with MSPs[8] are displayed by open blue circles. Their distribution broadly conforms to the relationship predicted by T. M. Tauris & G. J. Savonije (1999), depicted by the black solid and dashed lines representing the different chemical composition of the donor star. We also present the ELM WDs from sample S1, plotted as gray crosses on the diagram, which are commonly considered to be double WDs. This group of ELM WDs can be divided into two parts (Z. Li et al. 2019; W. R. Brown et al. 2020): the ELM WDs within the gray dashed box ($0.22\,M_\odot < M_{\rm WD} < 0.3\,M_\odot$, $P_{\rm orb} < 0.1$ day) may have evolved from the CE channels, which produce more massive He WDs (0.21–0.4 $M_\odot$) along with very short orbits; the remaining sources show positive correlation between mass and period, likely consistent with the RLO channels. The green solid line shows the best-fit curve based on a linear function, with slope and intercept values of 0.023(3) and 0.171(2), respectively. It can be seen that our nine high-priority ELM WDs roughly follow the evolutionary model of the RLO channel or T. M. Tauris & G. J. Savonije (1999).

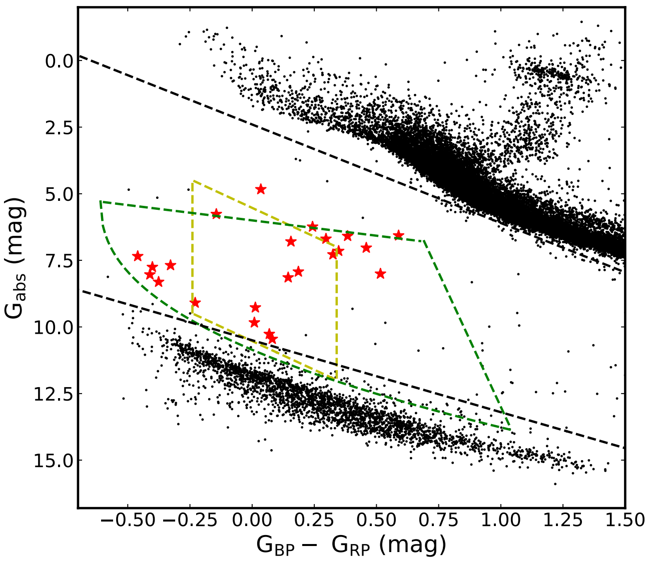

Figure 3. Distribution of 23 ELM WDs or candidates (marked by red stars) on the CMD. Black scatter points show the Gaia stars within 200 pc. The yellow dashed lines delineate the region where ELM WDs identified in the ELM Survey are predominantly located (A. Kosakowski et al. 2023a). The green dashed lines represent the selection region employed to search for ELM WD candidates based on Gaia DR2 data (I. Pelisoli & J. Vos 2019). Low-mass WD companions in MSP binaries are more likely to be found within two black dashed lines, as suggested by J. Antoniadis (2021).

4.4. Estimation of the Companion Mass

We select nine high-priority ELL-type ELM WDs listed in Table 2, and the mass of their unseen companions can be further estimated from the amplitude of ellipsoidal variations. The ZTF-g-band or r-band amplitude of ellipsoidal variation ($\cos 2\phi$ term) has been separated in the lightcurve fitting based on the five-parameter model in Section 3. Here, we only analyze the ellipsoidal variation amplitude in the g band. This amplitude, $A_{\rm EV}$, is principally determined by (S. L. Morris & S. A. Naftilan 1993; J. J. Hermes et al. 2014):

$$A_{\rm EV} = \frac{3\pi^2(15+\mu_1)(1+\tau_1)M_2R_1^3\sin^2 i}{5P_{\rm orb}^2(3-\mu_1)GM_1(M_1+M_2)}, \qquad (1)$$

where M_1 and R_1 are the mass and radius of the ELM WD, M_2 is the mass of unseen companion, and i is the orbital inclination angle. μ_1 and τ_1 are the linear limb-darkening coefficient and gravity-darkening coefficient of the primary, respectively. Here, we interpolate μ_1 from A. Claret et al. (2020), according to a given $T_{\rm eff}$ and $\log g_1$ in Table 1. The reference values from the SDSS-g' filter are employed, as it shares a similar central wavelength with the ZTF-g band. The temperature-dependent τ_1 is calculated by Equation (10) from S. L. Morris (1985).

The radius R_1 can be straightforwardly estimated using the known surface gravity g_1 and primary mass M_1:

$$R_1^2 = \frac{GM_1}{g_1}. \qquad (2)$$

Additionally, the mass function f_1(M2) derived from spectroscopy measurements is expressed as follows:

$$f_1(M_2) = \frac{P_{\rm orb}K_1^3}{2\pi G} = \frac{M_2^3\sin^3 i}{(M_1+M_2)^2}, \qquad (3)$$

where K_1 is the radial velocity amplitude of the optical primary.

---

[8] These confirmed MSP-ELM WDs can be obtained in Table A1 from I. Pelisoli & J. Vos (2019). We exclude the PSR J1959+2048, a black widow system containing a 0.035 $M_\odot$ companion. The very low mass of the companion may be attributed to ablation from the strong pulsar wind, which seems to be different from the population of normal MSP-WD systems. We also exclude PSR J2317+1439 and PSR J1853+1303 due to their excessively large error bars for the companion mass.

Table 2
The Measured and Derived Parameters of the Nine High-priority ELM WDs

No.	Name	R.A. (hh:mm:ss.ss)	Decl. (dd:mm:ss.s)	$T_{\rm eff}$ (K)	$\log g_1$ (cm s^{-2})	M_1 ($M_\odot$)	$\text{Parallax}_{\rm Gaia}$ (mas)	$\text{Parallax}_{\rm spec}$ (mas)	$\text{Distance}_{\rm spec}$ (kpc)
1	ZTF J0101+0401	01:01:28.69	+04:01:59.0	9284^{+120}_{-120}	$5.229^{+0.089}_{-0.089}$	0.188 ± 0.013	0.796 ± 0.098	0.803 ± 0.222	1.245 ± 0.321
2	ZTF J0404+0800	04:04:18.39	+08:00:02.9	$10,\ 860^{+120}_{-120}$	$4.985^{+0.121}_{-0.121}$	0.172 ± 0.014	1.742 ± 0.044	1.160 ± 0.229	0.862 ± 0.177
3	ZTF J0443+0541	04:43:02.66	+05:41:17.0	9390^{+140}_{-140}	$4.998^{+0.097}_{-0.097}$	0.159 ± 0.013	0.760 ± 0.085	0.708 ± 0.104	1.413 ± 0.211
4	ZTF J0745+1949	07:45:11.56	+19:49:26.6	8313^{+100}_{-100}	$6.151^{+0.074}_{-0.074}$	0.160 ± 0.010	1.088 ± 0.059	4.762 ± 0.941	0.210 ± 0.040
5	ZTF J0756+6704	07:56:10.73	+67:04:24.4	$11,\ 640^{+250}_{-250}$	$4.90^{+0.14}_{-0.14}$	0.181 ± 0.011	0.484 ± 0.046	0.626 ± 0.141	1.597 ± 0.343
6	ZTF J1048-0000	10:48:26.86	−00:00:56.8	8484^{+90}_{-90}	$5.831^{+0.051}_{-0.051}$	0.169 ± 0.016	0.641 ± 0.195	1.414 ± 0.373	0.707 ± 0.175
7	ZTF J1238+1946	12:38:00.08	+19:46:31.1	$14,\ 950^{+420}_{-420}$	$4.890^{+0.050}_{-0.050}$	0.197 ± 0.012	0.452 ± 0.099	0.344 ± 0.072	2.908 ± 0.583
8	ZTF J1401-0817	14:01:18.80	−08:17:23.5	8813^{+90}_{-90}	$5.731^{+0.048}_{-0.048}$	0.216 ± 0.042	0.823 ± 0.079	1.802 ± 1.135	0.555 ± 0.268
9	ZTF J1741+6526	17:41:40.49	+65:26:38.6	$10,\ 540^{+170}_{-170}$	$6.000^{+0.060}_{-0.060}$	0.170 ± 0.010	0.867 ± 0.143	1.049 ± 0.171	0.953 ± 0.151

Note. The values for spectrophotometric parallax ($\text{Parallax}_{\rm spec}$) or spectrophotometric distance ($\text{Distance}_{\rm spec}$) are taken from the references of the corresponding sources listed in Table 1.

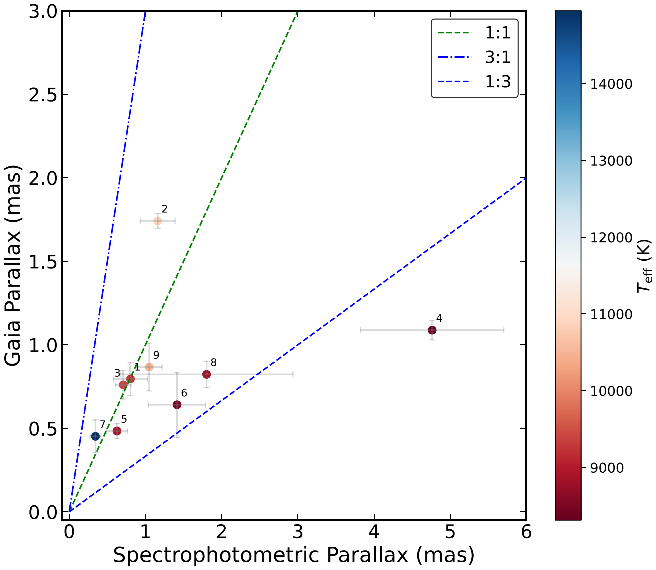

Figure 4. Spectrophotometric parallax estimates vs. Gaia parallaxes. The green dashed line denotes the 1:1 ratio line, while the blue dashed and dashed-dotted lines represent the 1:3 and 3:1 ratio lines, respectively. The color of the dots indicates different effective temperatures, and the numerical labels correspond to the source numbers in Table 2.

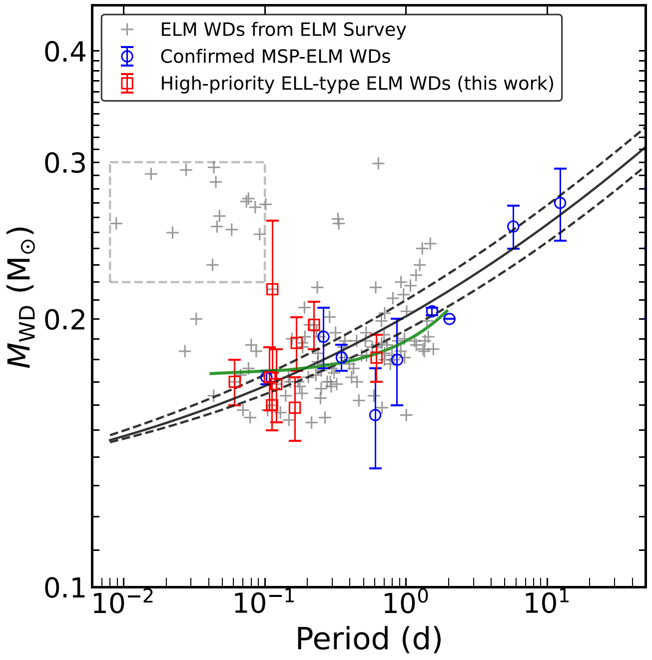

Figure 5. Mass–period distribution of ELM WDs. Nine high-priority ELL-type ELM WDs of our sample are plotted by open red squares. ELM WDs from sample S1 are depicted by gray crosses. The gray rectangular box marks the region corresponding to ELM WDs that should follow the CE channel. The green solid line represents the best-fit curve based on a linear function, for the gray crosses outside of the gray rectangle. Some confirmed MSP/ELM WDs are denoted by open blue circles, and they conform well to the relationships predicted in T. M. Tauris & G. J. Savonije (1999), as shown by solid and dashed lines with different chemical compositions (Pop. I, Pop. I+II, and Pop. II).

Therefore, solving Equations (1) and (3) simultaneously enables us to determine the values of the two unknowns: companion mass M_2 and inclination angle i.

In order to determine the effective range of values for M_2 and i, we perform 100,000 Monte Carlo (MC) simulations to numerically solve equations for seven targets with derived mass functions. For each simulation, the orbital period is fixed, while $A_{\rm EV}$, M_1, g_1, and $f_1(M_2)$ are randomly chosen from a Gaussian distribution within their respective measured uncertainties. The minimum mass of the secondary, $M_{2,\rm min}$, can be inferred from f_1(M2) by assuming an inclination angle of 90°. Meanwhile, the secondary is expected to be a WD or NS with a mass less than $3\,M_\odot$. So we only accept the solutions that have $M_{2,\rm min} < M_2 < 3\,M_\odot$ and $M_1 < 1.4\,M_\odot$. For instance, Figure 6 illustrates one- and two-dimensional projections for the valid solutions of J0745+1949. An obvious degeneracy exists between the companion mass M_2 and the inclination angle i.

It is noteworthy that only about 0.45% of simulations yield valid solutions for J0756+6704, which indicates the notable discrepancy between the measurements and the expected model. Nevertheless, we increase the number of MC simulations to 10^7 in order to obtain more available solutions to provide referable estimates.

For the remaining two sources lacking mass functions, their relationships between companion mass and orbital inclination, as inferred from Equation (1), are displayed in Figure 7. It can be observed that J0404+0800 is unlikely to host an NS unless the inclination angle is less than ∼20°. To give a referable value of M_2, we assume the orientation of the orbital angular momentum is arbitrary, equivalent to randomly sampling $\cos i$ between 0 and 1. Similarly, we employ 100,000 MC simulations to solve Equation (1) and accept the solutions that $M_2 < 3\,M_\odot$ and $M_1 < 1.4\,M_\odot$. The final constrained parameters

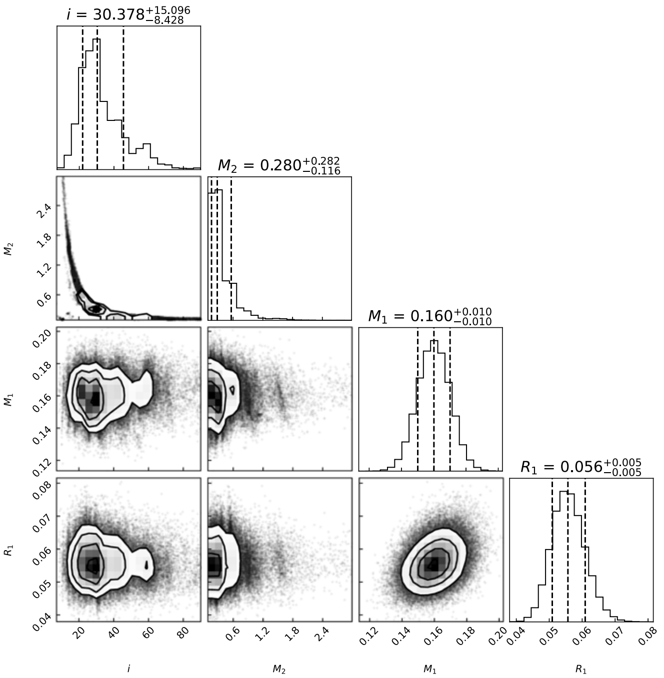

Figure 6. MC results of J0745+1949 for the joint distributions of four parameters (M_1, R_1, M_2, and i). The middle vertical dashed lines on the histograms indicate the median value, while the other two dashed lines represent the 1σ level.

(M_1, R_1, M_2, and i) of nine selected targets can be seen in Table 3.

The estimated parameters of J1741+6526 and J0745+1949 can be compared with the values reported in J. J. Hermes et al. (2014). We found the results of J1741+6526 agree well with the reported values. However, considerable disagreements emerge in the outcomes for J0745+1949. Specifically, our estimations for R_1 and i are notably smaller than the reported values ($R_1 \sim 0.176 R_\odot$, $i \sim 63^\circ\!.2$). In fact, our results are much closer to the values ($R_1 \sim 0.057 R_\odot$, $i \sim 10^\circ\!.5$) inferred from K. J. Bell et al. (2018).

In our estimations, the companion masses of four targets exceed $1\,M_\odot$, making them more likely candidates for harboring MSPs. However, for the other sources, the possibility of hosting MSPs still exists as long as the orbital inclination is smaller than expected. Follow-up radio or X-ray observations around ELM WDs can help confirm or eliminate the existence of MSPs (e.g., M. A. Agüeros et al. 2009; W. R. Brown et al. 2020).

4.5. Radio Pulse Search

Compared to normal pulsars, MSPs generally have larger radio beaming fractions, e.g., from 50% to 90% (M. Kramer et al. 1998), resulting in a high chance of detecting radio pulsations. In this study, we select six targets from Table 3 that have not yet been observed in radio, and perform radio observations for them by using Five-hundred-meter Aperture Spherical radio Telescope (FAST) in 2023 (PID: PT2023_0058), to search for potential pulse signals. Each target was carried out for a 15 minute L-band tracking observation, with the first minute dedicated to injecting modulated noise to calibrate the polarized pulse signal once the radio pulsations are discovered. The sampling time was chosen to be $\sim$50 μs, and the number of frequency channels was set to 4096.

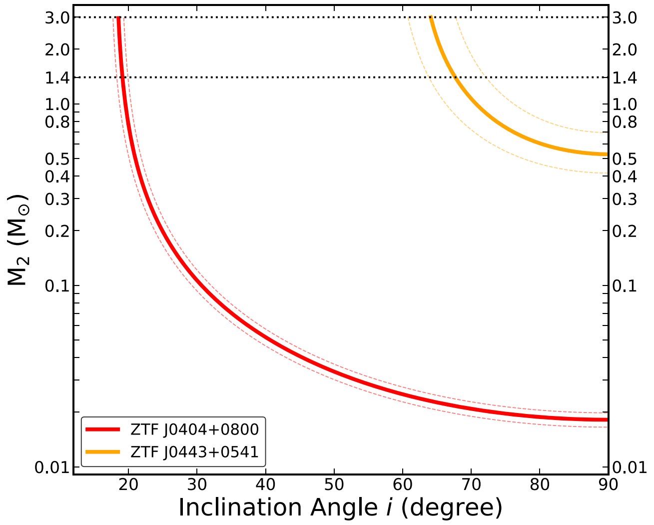

Figure 7. Companion mass M_2 vs. orbital inclination i for J0404+0800 and J0443+0541. The solid lines represent their relationships inferred from Equation (1), with other measured parameters fixed. The dashed lines depict the results when $A_{\rm EV}$ is increased or decreased by 1σ. Two black dotted lines indicate the isopleths for masses of $1.4\,M_\odot$ and $3\,M_\odot$.

The observational data were processed by `PRESTO`[9] (S. M. Ransom et al. 2002), one of the classic pulsar search software. First, the radio frequency interference were automatically eliminated, and then the data were dedispersed with the trial dispersion measures (DMs) ranging from 0 to 1000 pc cm^{-3}. Next, the time-domain signals were transformed into frequency-domain signals via fast Fourier transform. Afterward, the acceleration searches were executed with $z_{\rm max}$ (the maximum Fourier frequency derivative) of 200 to enhance sensitivity toward short-orbit systems.

However, no convincing radio pulse signal was found among these targets. The sensitivity can be estimated by the radiometer equation:

$$S_{\rm min} = \frac{({\rm S/N})_{\rm min}(T_{\rm sys} + T_{\rm sky})}{G\sqrt{n_{\rm p} t_{\rm int} \Delta f}} \times \sqrt{\frac{\delta}{1-\delta}}, \tag{4}$$

where $({\rm S/N})_{\rm min}$ is threshold of signal-to-noise ratio, $T_{\rm sys}$ is the system temperature, $T_{\rm sky}$ is the sky background temperature, G is the antenna gain, $T_{\rm int}$ is the integration time, n_p is the number of polarizations, Δf is the observed bandwidth and δ is the duty cycle of pulse.

For FAST L-band observations with a central frequency of 1250 MHz, $T_{\rm sys} = 24$ K, $G = 16$ K Jy^{-1} and $n_p = 2$. The actual integration time $T_{\rm int}$ of each target is 840 s. The effective bandwidth Δf is 400 MHz. The sky background temperature $T_{\rm sky}$ at 1400 MHz is inferred from the 408-MHZ All-Sky Continuum Survey (C. G. T. Haslam et al. 1982). To evaluate δ, we utilize the mean value (0.29) of $W_{10}/P_{\rm spin}$ for MSPs orbited by He WDs, collected from ATNF v1.70 catalog[10] (R. N. Manchester et al. 2005), where W_{10} represents the pulse width at 10% level of the peak and $P_{\rm spin}$ is the spin period. Applying the parameters mentioned above, the upper limit of radio flux $S_{\rm min}$ at 1400 MHz can be estimated to be $\sim$8 μJy

---

[9] https://github.com/scottransom/presto

[10] https://www.atnf.csiro.au/research/pulsar/psrcat/

Table 3
Parameters Constrained from MC Simulations and Radio Observations for Nine Selected Targets

Name	M_1 ($M_\odot$)	R_1 ($R_\odot$)	M_2 ($M_\odot$)	i (°)	$A_{\rm EV}$ (%)	$T_{0,{\rm sup\_conj}}$ (MJD)	μ	τ	$f_1(M_2)$ ($M_\odot$)	Radio	$L_{1400\ {\rm MHz}}$ (mJy kpc^2)
ZTF J0101+0401	$0.193^{+0.011}_{-0.011}$	$0.191^{+0.013}_{-0.014}$	$0.635^{+0.987}_{-0.233}$	$47.049^{+23.971}_{-17.740}$	1.32(16)	58281.49558	0.53	0.27	0.151(19)	FAST	<0.0139
ZTF J0404+0800	$0.172^{+0.014}_{-0.014}$	$0.222^{+0.034}_{-0.030}$	$0.027^{+0.044}_{-0.013}$	$61.829^{+19.544}_{-24.274}$	1.11(09)	58206.17723	0.51	0.74	⋯	FAST	<0.0058
ZTF J0443+0541	$0.160^{+0.013}_{-0.013}$	$0.224^{+0.023}_{-0.018}$	$0.421^{+0.697}_{-0.227}$	$74.819^{+10.491}_{-13.938}$	2.69(16)	58334.53492	0.54	0.27	⋯	FAST	<0.0156
ZTF J0745+1949	$0.160^{+0.010}_{-0.010}$	$0.056^{+0.005}_{-0.005}$	$0.280^{+0.282}_{-0.116}$	$30.378^{+15.096}_{-8.428}$	1.61(09)	58205.18216	0.55	0.30	0.017(3)	FAST	<0.0003
ZTF J0756+6704	$0.181^{+0.011}_{-0.008}$	$0.321^{+0.036}_{-0.096}$	$1.326^{+1.190}_{-0.437}$	$54.169^{+27.036}_{-15.451}$	0.90(08)	58207.49116	0.48	0.70	0.546(33)	GBT	<0.2550
ZTF J1048-0000	$0.191^{+0.010}_{-0.020}$	$0.087^{+0.007}_{-0.007}$	$0.679^{+0.179}_{-0.032}$	$76.152^{+9.840}_{-16.545}$	8.42(78)	58199.31062	0.55	0.29	0.383(31)	FAST	<0.0039
ZTF J1238+1946	$0.195^{+0.012}_{-0.012}$	$0.260^{+0.020}_{-0.014}$	$1.327^{+0.695}_{-0.330}$	$50.050^{+9.887}_{-9.870}$	2.44(14)	58202.43981	0.42	0.58	0.453(14)	GBT	<0.0552
ZTF J1401-0817	$0.269^{+0.009}_{-0.005}$	$0.117^{+0.008}_{-0.010}$	$1.167^{+0.902}_{-0.297}$	$58.778^{+20.141}_{-17.158}$	10.37(16)	58203.46077	0.53	0.28	0.487(12)	FAST	<0.0024
ZTF J1741+6526	$0.174^{+0.003}_{-0.002}$	$0.064^{+0.004}_{-0.003}$	$1.150^{+0.190}_{-0.049}$	$78.113^{+9.248}_{-12.204}$	1.42(11)	58197.39962	0.50	0.75	0.801(39)	GBT	<0.0908

Note. Four main parameters (M_1, R_1, M_2, and i) are constrained from MC simulations, as described in Section 4.4. $A_{\rm EV}$ is the amplitude of ellipsoidal variation separated from ZTF-g-band lightcurves. $T_{0,{\rm sup\_conj}}$ is the referenced epoch corresponding to the superior conjunction of the ELM WD. μ_1 and τ_1 are the linear limb-darkening coefficient and gravity-darkening coefficient used in MC simulations. Mass function $f_1(M_2)$ is calculated from Equation (3), and the related parameters are provided from the References listed in Table 1. The "Radio" column indicates the telescopes used for radio searches. Specifically, six sources were observed with FAST in this work, while three sources were observed using the GBT with no radio pulsations found (W. R. Brown et al. 2020; T. M. Athanasiadis et al. 2021). $L_{1400\ {\rm MHz}}$ represents the upper limit of radio luminosity at 1400 MHz.

when the expected $({\rm S/N})_{\rm min}$ is 7 and the spectral index is assumed to be -1.4 (S. D. Bates et al. 2013). Then, the upper limit of pseudo luminosity, $L_{1400\ {\rm MHz}}$, can be calculated by $S_{\rm min}d^2$, where d is the spectrophotometric distance. It is noteworthy that the nondetection of radio pulsations could also be attributed to some factors, such as the emission beam failing to point toward Earth, or the radio signals being obscured by the companion star.

On the other hand, MSPs also exhibit abundant thermal or nonthermal X-ray emissions, originating from the heated polar cap, magnetosphere, and intrabinary shock, and their X-ray luminosity has been found to be positively correlated with spin-down luminosity (J. Lee et al. 2018, 2023). We have also crossmatched our targets with X-ray catalogs, such as Swift 2SXPS,[11] 4XMM DR13,[12] and Chandra Source Catalog release 2.1,[13] within a search radius of 1′. Still, no X-ray counterpart was found. Combining the results of radio and X-ray searches, these six targets seem to resemble double WDs rather than MSP/WD systems.

5. Constraining the Fraction of Ellipsoidal ELM WD/MSP Systems

Many attempts to search for MSPs around low-mass WDs have been unsuccessful, supporting the view that the fraction of MSPs hosting in low-mass WD binary systems should be intrinsically low. R. Schneider et al. (2001) predict the birth rate of double WDs is two orders of magnitude higher than that of NS/WD systems. In fact, a considerable fraction of pulsar binaries may be disrupted during supernova explosions due to excessive mass loss or high kick velocities. J. J. Andrews et al. (2014) suggested that most low-mass WDs are accompanied by CO-core WD companions by using a mixture Gaussians model, and the NS companion fraction $f_{\rm NS}$ is estimated to be <16% within 1σ uncertainty. T. M. Athanasiadis et al. (2021) inferred that the $f_{\rm NS}$ is even less than 10%, based on the nondetection of radio signals for a group of low-mass WD binaries.

In this study, our primary focus is on examining the fraction ($f_{\rm MSP,ELL}$) of ELM WDs with observable ellipsoidal variations orbited by MSP companions, based on the fact that no radio pulsations were detected. Similar to the method described in J. van Leeuwen et al. (2007) and M. A. Agüeros et al. (2009), the expected $f_{\rm MSP,ELL}$ can be simply estimated by using

$$\prod_{j=1}^{N}(1 - P_{\rm beam}\times P_{L,j}\times P_{\rm eff}\times f_{\rm MSP,ELL}) > \frac{1}{2}, \qquad (5)$$

where $P_{\rm beam}$ is the radio beaming fraction, $P_{L,j}$ represents the radio luminosity completeness of jth source, and $P_{\rm eff}$ denotes the success rate of pulsar search algorithm.

We assume $P_{\rm beam}$ of MSPs to be 0.7 ± 0.2 (M. Kramer et al. 1998), and $P_{\rm eff}$ is set to a modest value of 0.8. To determine the $P_{L,j}$, the underlying luminosity distribution of MSPs should be known at first, which is still unclear at present. Here, we employ the log-normal luminosity distribution with $\mu = -1.1$ and $\sigma = 0.9$ (C.-A. Faucher-Giguère & V. M. Kaspi 2006), which are widely applied in the population synthesis study of pulsars. Then, each $P_{L,j}$ can be calculated as the proportion of luminosity exceeding $L_{1400\ {\rm MHz}}$ within the underlying luminosity distribution.

There are nine sources listed in Table 3, which have been observed by FAST or Green Bank Telescope (GBT), enabling the calculation of $f_{\rm MSP,ELL}$. In addition, we incorporate two sources, J0056-0611 and J0112+1835, which exhibit ellipsoidal variation[14] and were observed by GBT (K. J. Bell et al. 2018; W. R. Brown et al. 2020). Their $L_{1400\ {\rm MHz}}$ are inferred to be <0.0552 mJy kpc^2 by using the assumed spectral index of -1.4. Combining the results of 11 ellipsoidal ELM WDs, the estimated $f_{\rm MSP,ELL}$ is below $15^{+6}_{-3}\%$. It is worth noting that we did not consider the effects of assumed spin periods and DM on sensitivity (M. A. Agüeros et al. 2009; T. M. Athanasiadis et al. 2021), which could lead to an underestimation of the $f_{\rm MSP,ELL}$. On the other hand, if the luminosity of the MSP population is dimmer than the assumed distribution (e.g., W. J. Huang & H. G. Wang 2020), or if the adopted spectrophotometric distances for some targets (e.g., J1048-0000, 1401-0817, and

---

[11] https://www.swift.ac.uk/2SXPS/

[12] http://xmmssc.irap.omp.eu/Catalogue/4XMM-DR13/4XMM_DR13.html

[13] https://cxc.cfa.harvard.edu/csc/

[14] Note that their ellipsoidal visibility was not found in the ZTF data.

J0745+1949) are underestimated, leading to an overestimation of radio luminosity completeness, the $f_{\mathrm{MSP,ELL}}$ will also be underestimated. It is expected that the $f_{\mathrm{MSP,ELL}}$ is slightly larger than f_{NS}, as ELM WDs are more easily tidally distorted by heavier MSPs than CO-core WDs in similar orbits, thereby exhibiting ellipsoidal variations. However, if the intrinsic f_{NS} is sufficiently small, the difference may be negligible. Incorporating more ellipsoidal ELM WDs would provide better constraints on $f_{\mathrm{MSP,ELL}}$.

6. Conclusion

ELM WDs may be tidally distorted by their heavier companions (e.g., MSPs or CO-core WD), leading to discernible ellipsoidal variations in time-series data. Identifying such systems can aid in the search for potential MSPs. In this study, we selected approximately 12,000 samples of ELM WDs and their candidates, and eventually identified 23 targets exhibiting ellipsoidal-like variations with orbital periods shorter than 1 day, using the public data from ZTF DR15. And 17 of them are newly discovered.

We further selected nine high-priority targets that are likely consistent with the evolution of the RLO channel on the mass–period diagram as well as have well-measured atmospheric parameters. Their companion masses are estimated from the extracted ellipsoidal variation amplitude. According to our estimation, four of them have companion masses exceeding 1 $M_{\odot}$, making them more likely candidates for harboring MSPs. Although for other sources, we cannot completely rule out the possibility that they host MSPs.

The FAST observations were then performed on six targets of them to search for their potential radio pulsations, but no convincing pulse signals were detected. Their upper limit of radio flux at 1400 MHz is about 8 μJy, estimated using the radiometer equation. Combining the fact that their counterparts were not found in some X-ray catalogs, these systems are more likely to be double WDs. Based on the nondetection of radio pulsations by GBT or FAST from 11 similar systems, the fraction of ellipsoidal ELM WDs around MSPs ($f_{\mathrm{MSP,ELL}}$) is estimated to be $<15^{+6}_{-3}\%$.

We anticipate that further multiwavelength observations and studies of remaining ELL-type targets in this work, as well as newly discovered ellipsoidal ELM WDs from other research (e.g., L. Ren et al. 2023), can increase the chances of finding MSPs or better constrain the fraction of ellipsoidal ELM WDs around MSPs. Besides, about 4300 candidates from our initial sample have a decl. $< -30°$ and are not covered by the ZTF's footprint. These sources are expected to be searched for periodic signals using southern telescopes, such as the Large Synoptic Survey Telescope, in the future.

Acknowledgments

We acknowledge the use of public lightcurve data from ZTF obtained through IRSA ZTF-LC-API queries (https://irsa.ipac.caltech.edu/docs/program_interface/ztf_lightcurve_api.html) and public astrometric parameters from Gaia archive (https://gea.esac.esa.int/archive/). The VizieR catalogs and the ATNF pulsar catalog were also utilized for this work. This work made use of the data from FAST (Five-hundred-meter Aperture Spherical radio Telescope, https://cstr.cn/31116.02.FAST). FAST is a Chinese national mega-science facility, operated by National Astronomical Observatories, Chinese Academy of Sciences. We acknowledge the science research grants from the China Manned Space Project. W.J.H. and P.H.T. thank the support from the National Natural Science Foundation of China (NSFC) under grant 12273122. L.L.R. and J.M.L. gratefully acknowledge support from the NSFC through grant 12233013.

Software: `Astropy` (Astropy Collaboration et al. 2013, 2018), `PRESTO` (S. M. Ransom et al. 2002).

ORCID iDs

W. J. Huang https://orcid.org/0000-0001-5546-8549
Pak-Hin Thomas Tam https://orcid.org/0000-0002-1262-7375
L. L. Ren https://orcid.org/0000-0002-1428-4003
J. M. Lin https://orcid.org/0009-0008-9942-620X

References

Agüeros, M. A., Camilo, F., Silvestri, N. M., et al. 2009, ApJ, 697, 283
Althaus, L. G., Miller Bertolami, M. M., & Córsico, A. H. 2013, A&A, 557, A19
Andrews, J. J., Price-Whelan, A. M., & Agüeros, M. A. 2014, ApJL, 797, L32
Antoniadis, J. 2021, MNRAS, 501, 1116
Antoniadis, J., Freire, P. C. C., Wex, N., et al. 2013, Sci, 340, 448
Antoniadis, J., van Kerkwijk, M. H., Koester, D., et al. 2012, MNRAS, 423, 3316
Arzoumanian, Z., Brazier, A., Burke-Spolaor, S., et al. 2018, ApJS, 235, 37
Astropy Collaboration, Price-Whelan, A. M., Sipőcz, B. M., et al. 2018, AJ, 156, 123
Astropy Collaboration, Robitaille, T. P., Tollerud, E. J., et al. 2013, A&A, 558, A33
Athanasiadis, T. M., Berezina, M., Antoniadis, J., et al. 2021, MNRAS, 505, 4981
Bassa, C. G., Antoniadis, J., Camilo, F., et al. 2016, MNRAS, 455, 3806
Bassa, C. G., van Kerkwijk, M. H., Koester, D., & Verbunt, F. 2006, A&A, 456, 295
Bassa, C. G., van Kerkwijk, M. H., & Kulkarni, S. R. 2003, A&A, 403, 1067
Bates, S. D., Lorimer, D. R., & Verbiest, J. P. W. 2013, MNRAS, 431, 1352
Bell, K. J., Hermes, J. J., & Kuszlewicz, J. S. 2018, arXiv:1809.05623
Bellm, E. C., Kulkarni, S. R., Graham, M. J., et al. 2019, PASP, 131, 018002
Brown, W. R., Gianninas, A., Kilic, M., Kenyon, S. J., & Allende Prieto, C. 2016, ApJ, 818, 155
Brown, W. R., Kilic, M., Allende Prieto, C., & Kenyon, S. J. 2010, ApJ, 723, 1072
Brown, W. R., Kilic, M., & Gianninas, A. 2017, ApJ, 839, 23
Brown, W. R., Kilic, M., Kosakowski, A., & Gianninas, A. 2022, ApJ, 933, 94
Brown, W. R., Kilic, M., Kosakowski, A., et al. 2020, ApJ, 889, 49
Cadelano, M., Ferraro, F. R., Istrate, A. G., et al. 2019, ApJ, 875, 25
Cadelano, M., Pallanca, C., Ferraro, F. R., et al. 2015, ApJ, 812, 63
Claret, A., Cukanovaite, E., Burdge, K., et al. 2020, A&A, 634, A93
Demorest, P. B., Pennucci, T., Ransom, S. M., Roberts, M. S. E., & Hessels, J. W. T. 2010, Natur, 467, 1081
Desvignes, G., Caballero, R. N., Lentati, L., et al. 2016, MNRAS, 458, 3341
Durant, M., Kargaltsev, O., Pavlov, G. G., et al. 2012, ApJ, 746, 6
El-Badry, K., Rix, H.-W., Quataert, E., Kupfer, T., & Shen, K. J. 2021, MNRAS, 508, 4106
Faucher-Giguère, C.-A., & Kaspi, V. M. 2006, ApJ, 643, 332
Freire, P. C. C., Wolszczan, A., van den Berg, M., & Hessels, J. W. T. 2008, ApJ, 679, 1433
Gentile Fusillo, N. P., Tremblay, P. E., Cukanovaite, E., et al. 2021, MNRAS, 508, 3877
Gianninas, A., Curd, B., Fontaine, G., Brown, W. R., & Kilic, M. 2016, ApJL, 822, L27
Gianninas, A., Hermes, J. J., Brown, W. R., et al. 2014, ApJ, 781, 104
Gianninas, A., Kilic, M., Brown, W. R., Canton, P., & Kenyon, S. J. 2015, ApJ, 812, 167
Graham, M. J., Kulkarni, S. R., Bellm, E. C., et al. 2019, PASP, 131, 078001
Haslam, C. G. T., Salter, C. J., Stoffel, H., & Wilson, W. E. 1982, A&AS, 47, 1
Heber, U. 2009, ARA&A, 47, 211
Hermes, J. J., Brown, W. R., Kilic, M., et al. 2014, ApJ, 792, 39
Huang, S.-J., Hu, Y.-M., Korol, V., et al. 2020, PhRvD, 102, 063021
Huang, W. J., & Wang, H. G. 2020, ApJ, 905, 144
Istrate, A. G., Marchant, P., Tauris, T. M., et al. 2016, A&A, 595, A35
Istrate, A. G., Tauris, T. M., & Langer, N. 2014a, A&A, 571, A45

Istrate, A. G., Tauris, T. M., Langer, N., & Antoniadis, J. 2014b, A&A, 571, L3
Jacoby, B. A., Hotan, A., Bailes, M., Ord, S., & Kulkarni, S. R. 2005, ApJL, 629, L113
Kaplan, D. L., Bhalerao, V. B., van Kerkwijk, M. H., et al. 2013, ApJ, 765, 158
Kaplan, D. L., Stovall, K., Ransom, S. M., et al. 2012, ApJ, 753, 174
Keller, P. M., Breedt, E., Hodgkin, S., et al. 2021, MNRAS, 509, 4171
Kepler, S. O., Pelisoli, I., Koester, D., et al. 2019, MNRAS, 486, 2169
Kilic, M., Hermes, J. J., Córsico, A. H., et al. 2018, MNRAS, 479, 1267
Kilic, M., Hermes, J. J., Gianninas, A., & Brown, W. R. 2015, MNRAS, 446, L26
Koljonen, K. I. I., & Linares, M. 2023, MNRAS, 525, 3963
Kosakowski, A., Brown, W. R., Kilic, M., et al. 2023a, ApJ, 950, 141
Kosakowski, A., Kupfer, T., Bergeron, P., & Littenberg, T. B. 2023b, ApJ, 959, 114
Kramer, M., Xilouris, K. M., Lorimer, D. R., et al. 1998, ApJ, 501, 270
Kupfer, T., Korol, V., Shah, S., et al. 2018, MNRAS, 480, 302
Lee, J., Hui, C. Y., Takata, J., et al. 2018, ApJ, 864, 23
Lee, J., Hui, C. Y., Takata, J., et al. 2023, ApJ, 944, 225
Li, Z., Chen, X., Chen, H.-L., & Han, Z. 2019, ApJ, 871, 148
Limoges, M. M., Bergeron, P., & Dufour, P. 2009, ApJ, 696, 1461
Linares, M. 2020, in Proc. of Science, Vol. 362, Multifrequency Behaviour of High Energy Cosmic Sources - XIII (MULTIF2019) (Trieste: SISSA), 23
Manchester, R. N., Hobbs, G. B., Teoh, A., & Hobbs, M. 2005, AJ, 129, 1993
Masci, F. J., Laher, R. R., Rusholme, B., et al. 2019, PASP, 131, 018003
Mata Sánchez, D., Istrate, A. G., van Kerkwijk, M. H., Breton, R. P., & Kaplan, D. L. 2020, MNRAS, 494, 4031
Maxted, P. F. L., Bloemen, S., Heber, U., et al. 2014, MNRAS, 437, 1681
Morris, S. L. 1985, ApJ, 295, 143
Morris, S. L., & Naftilan, S. A. 1993, ApJ, 419, 344
Pelisoli, I., & Vos, J. 2019, MNRAS, 488, 2892
Ransom, S. M., Eikenberry, S. S., & Middleditch, J. 2002, AJ, 124, 1788
Rebassa-Mansergas, A., Hollands, M., Parsons, S. G., et al. 2024, A&A, 686, A221
Reindl, N., Schaffenroth, V., Filiz, S., et al. 2021, A&A, 647, A184
Ren, L., Li, C., Ma, B., et al. 2023, ApJS, 264, 39
Schneider, R., Ferrari, V., Matarrese, S., & Portegies Zwart, S. F. 2001, MNRAS, 324, 797
Splaver, E. M., Nice, D. J., Stairs, I. H., Lommen, A. N., & Backer, D. C. 2005, ApJ, 620, 405
Sun, M., & Arras, P. 2018, ApJ, 858, 14
Tauris, T. M., & Savonije, G. J. 1999, A&A, 350, 928
van Kerkwijk, M. H., Bassa, C. G., Jacoby, B. A., & Jonker, P. G. 2005, in ASP Conf. Ser. 328, Binary Radio Pulsars, ed. F. A. Rasio & I. H. Stairs (San Francisco, CA: ASP), 357
van Kerkwijk, M. H., Bell, J. F., Kaspi, V. M., & Kulkarni, S. R. 2000, ApJL, 530, L37
van Kerkwijk, M. H., Bergeron, P., & Kulkarni, S. R. 1996, ApJL, 467, L89
van Leeuwen, J., Ferdman, R. D., Meyer, S., & Stairs, I. 2007, MNRAS, 374, 1437
Verbiest, J. P. W., Bailes, M., van Straten, W., et al. 2008, ApJ, 679, 675
Wang, K., Németh, P., Luo, Y., et al. 2022, ApJ, 936, 5
Wei, N., Xu, K., Gao, Z.-F., Jiang, L., & Chen, W.-C. 2024, ApJ, 962, 54
Yuan, H., Li, Z., Bai, Z., et al. 2023, AJ, 165, 119